ARTICLE

Au Nanorice Assemble Electrolytically into Mesostars

Rizia Bardhan,[†,§] Oara Neumann,[‡,§] Nikolay Mirin,[†,§] Hui Wang,[†,§] and Naomi J. Halas[†,‡,§,*]

[†]Department of Chemistry, [‡]Department of Electrical and Computer Engineering, and [§]Laboratory for Nanophotonics, Rice University, Houston, Texas 77005

ABSTRACT Star-shaped mesotructures are formed when an aqueous suspension of Au nanorice particles, which consist of prolate hematite cores and a thin Au shell, is subjected to an electric current. The nanorice particles assemble to form hyperbranched micrometer-scale mesostars. To our knowledge, this is the first reported observation of nanoparticle assembly into larger ordered structures under the influence of an electrochemical process (H_2O electrolysis). The assembly is accompanied by significant modifications in the morphology, dimensions, chemical composition, crystallographic structure, and optical properties of the constituent nanoparticles.

KEYWORDS: mesostars · nanorice · α-FeOOH · α-Fe_2O_3 · electrolysis-induced self-assembly

The assembly of materials and structures from constituent nanoparticles is currently an important topic of fundamental research, stimulated by the growth of numerous applications such as new optical devices,[1,2] chemical sensing,[3,4] composite materials,[5] catalysis,[6] and biomedicine.[7,8]

The design and synthesis of novel nanoparticles has been an important starting point, since nanoscale size, shape, and morphology determine the properties of larger materials assembled from nanoscale substituents. The hierarchical self-assembly of nanoscale building blocks can lead to the formation of complex supramolecular assemblies, frequently in striking similarity to structure formation in biological systems.

Here we report a surprising observation of the formation of mesoscale star-shaped particles with a hierarchical substructure when an aqueous suspension of nanorice particles[9] is subjected to electrolysis. This unusual electrolytically assisted assembly is distinct from other electrochemically driven processes, such as the electrochemical synthesis of metal or metal oxide structures.[10,11] In this case, electrolysis transforms both the shape and composition of the nanorice particles. The nanorice particles consist of a prolate iron oxide (hematite, α-Fe_2O_3) core coated with a thin Au shell, where the hyperbranched mesostars were composed of Au, iron oxide, and iron oxyhydroxide (goethite, α-FeOOH). To the best of our knowledge, the process of electrolyzing an aqueous suspension to transform nanoparticles into mesoscale structures has not been previously reported. This discovery may provide a new approach for the development of new structures and materials from nanoscale constituents.

RESULTS AND DISCUSSION

The electrolytic cell utilized to form the mesostars is shown in Scheme 1. Platinum electrodes 0.020 mm wide were placed 0.014 m apart in an aqueous suspension of nanorice particles (10^9 particles/mL) and connected to a DC power supply. The nanorice particles utilized in these experiments consisted of prolate hematite cores with a longitudinal diameter of 340 ± 25 nm and a transverse diameter of 54 ± 6 nm, coated with a 22 ± 3 nm Au shell. At ambient temperature and pressure, a potential difference of 5 V was applied to the cell, and the particles self-assembled to form mesostars within 24 h. The mesostars were characterized using several analytical techniques to elucidate their formation mechanism, including electron microscopy, crystallography, and UV−vis spectroscopy.

The mesostars were typically 650 ± 80 nm in length and width and ~380 ± 30 nm in height, as shown in the scanning electron microscope (SEM) image in Figure 1A. All the mesostars observed in solution had similar shape and morphology but varied in size distribution. Powder X-ray diffraction (XRD) studies (Figure 1B) revealed a sur-

*Address correspondence to halas@rice.edu.

Received for review October 5, 2008 and accepted December 30, 2008.

Published online January 7, 2009. 10.1021/nn800657t CCC: $40.75

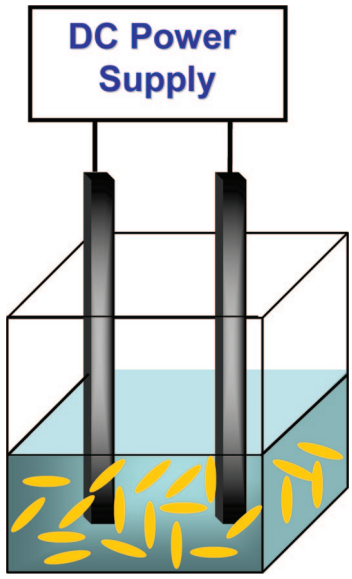

Scheme 1. Schematic representation of experimental set-up showing a DC power supply connected between two Pt electrodes (gray bars), separated by 0.014 m, immersed in aqueous Au nanorice solution.

prising transformation in the composition and crystal structure of the mesostars relative to the nanorice particles. XRD spectrum of α-Fe_2O_3 particles, which served as the core material of the nanorice is shown in Figure 1B-i. These particles show a highly crystalline, hexagonal phase of α-Fe_2O_3 with cell parameters a = 5.035 Å and c = 13.747 Å and space group *R*3*c* (No. 167) (JCPDS card no. 98-000-0240). The XRD peak intensities correlate well with those from the powder diffraction intensity profile of α-Fe_2O_3. However, a preferential orientation of the α-Fe_2O_3 core particles is observed, a common feature among single crystalline nanoparticles. The XRD spectrum of nanorice (Figure 1B-ii) clearly demonstrates the presence of a crystalline Au shell covering the α-Fe_2O_3 cores. The crystal structure of the Au shell corresponds to the cubic phase of Au with cell parameters a = 4.078 Å and space group *Fm*3*m* (No. 225) (JCPDS card no. 98-000-0230). The Au shell on the α-Fe_2O_3 cores grows non-epitaxially as a polycrystal, which explains the absence of preferential orientation in the XRD spectrum of nanorice. The XRD spectrum of mesostars (Figure 1B-iii) reveals a mixture of peaks corresponding to α-FeOOH, α-Fe_2O_3, and Au. The α-FeOOH peaks suggest a partial transformation of α-Fe_2O_3 into α-FeOOH, which has an orthorhombic phase with lattice parameters a = 4.937 Å, b = 4.432 Å, and c = 2.994 Å, and space group *P*21*nm* (No. 31) (JCPDS card no. 00-026-0792). The strongest peak corresponding to the α-FeOOH (101) plane indicates that the mesostars are mostly composed of goethite, and also specifies a preferential orientation of the goethite crystalline domains. (See Supporting Information Figure S1 for the XRD intensity profiles of the corresponding JCPD card no. mentioned above.)

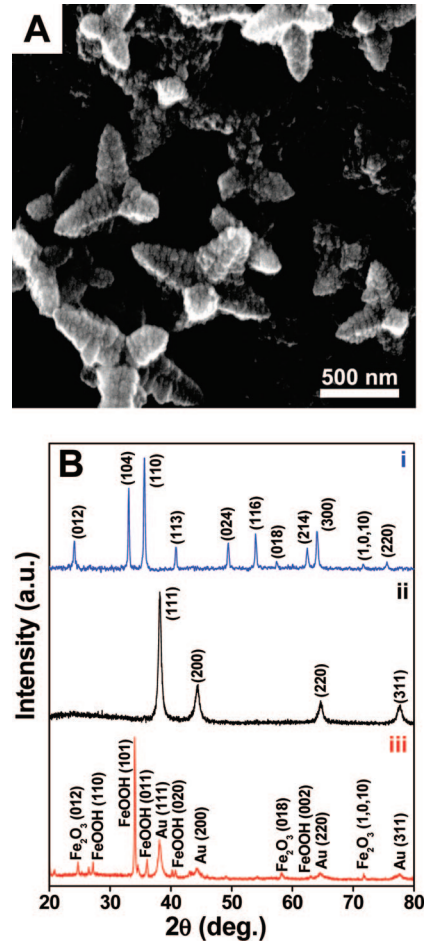

Figure 1. Electron microscopy and crystallographic studies of mesostars prepared at 5 V. (A) SEM image of Mesostars. (B) XRD spectra of (i) α-Fe_2O_3 cores, (ii) nanorice (showing Au peaks), and (iii) mesostars. The spectra are offset for clarity.

The observed alteration in structure and composition of nanorice particles to form mesostars was further studied using transmission electron microscopy (TEM) and electron diffraction (ED). TEM images with corresponding ED and selected area electron diffraction (SAED) patterns of mesostars are shown in Figure 2. A smaller star-shaped structure obtained within 6 h of electrolysis is shown in Figure 2A. The observed mesostar was polycrystalline as suggested by the ED ring pattern. The TEM micrograph and corresponding SAED pattern of a mesostar formed after 24 h of electrolysis is shown in Figure 2B. The SAED pattern demonstrates an orthorhombic single crystalline area that is oriented toward the (200) plane and corresponds to α-FeOOH. In addition to the mesostars, α-FeOOH nanocrystals were observed in the solution mixture (Figure 2C). These nanocrystals demonstrated the orthorhombic phase of α-FeOOH that is preferentially oriented toward the [001] direction. The tips of the mesostars, shown in Figure 2D, also consisted of single crystalline domains of α-FeOOH oriented along the (200) plane. Dark-field TEM, an effective tool in observing lattice defects, grain boundaries, and ordered domain structures, was uti-

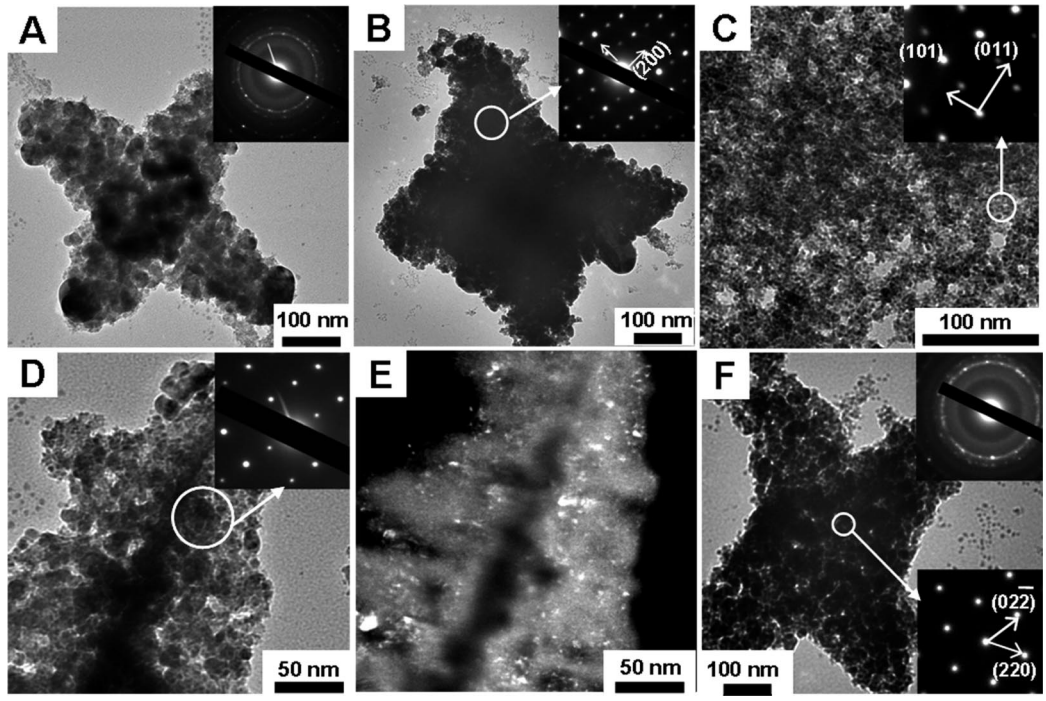

Figure 2. TEM micrographs of (A) a star-shaped structure obtained after 6 h of electrolysis and ED pattern showing polycrystalline rings provided as inset, (B) a mesostar formed after 24 h of electrolysis and corresponding SAED pattern representing orthorhombic α-FeOOH single crystalline domain, (C) an α-FeOOH nanocrystals observed in solution and SAED pattern showing orthorhombic α-FeOOH single crystalline domain, (D) tip of a mesostar and corresponding SAED pattern representing orthorhombic α-FeOOH single crystalline area, (E) dark field image of mesostar tip corresponding to panel D, and (F) mesostar obtained after 24 h of electrolysis; ED pattern showing polycrystalline rings provided as top inset, and SAED pattern representing cubic Au single crystalline area provided as bottom inset. The selected area corresponding to the SAED patterns in panels B—D,F are shown in circle.

lized to image the mesostar tip as shown in Figure 2E. The highly crystalline α-FeOOH domains are clearly demarcated by the lighter areas in Figure 2E. The darker central area indicates that this region is relatively dense and does not allow the electron beam to penetrate through. The TEM micrographs and SAED patterns in Figure 2A—E undoubtedly show that these mesostars have many crystalline domains of α-FeOOH, which explains the α-FeOOH peaks observed in the XRD spectrum of mesostars (Figure 1B-iii). The chemical composition of the observed mesostars was generally identical, composed mostly of α-FeOOH crystalline domains. However, the mesostars are also composed of Au as indicated by the XRD spectrum. A single mesostar is shown in Figure 2F. While its ED pattern (top inset) illustrates polycrystallinity, its SAED pattern (bottom inset) shows a face-centered cubic single crystalline domain of Au oriented along the (220) plane. Since these mesostructures were polycrystalline, individual crystallographic domains of Au, α-FeOOH, and α-Fe_2O_3 are difficult to determine for each particle; however, these representative TEM images confirm their composition.

The phase transformation of α-FeOOH to α-Fe_2O_3 is known to occur *via* heat treatment by loss of H_2O molecules[14] or by liquid phase transformation.[15] However, at present the reverse mechanism of α-Fe_2O_3 conversion to α-FeOOH is not well understood. The formation of α-FeOOH nanocrystals is strongly influenced by the presence of anions in solution, the temperature of the reaction mixture, the pH, and the oxidizing agents.[12,13] The shape and size of α-FeOOH nanocrystals influence many of their physical properties, which consequently determine the morphological development of larger-ordered structures. The formation mechanism discussed below explains the morphological modification as well as the alteration in the composition of α-Fe_2O_3-Au nanorice particles to form mesostars composed of α-Fe_2O_3, Au, and α-FeOOH.

A systematic and controlled study of mesostar formation revealed electrolysis-induced complex assembly of nanorice particles to form these hierarchical structures. A schematic representation of the mesostar formation mechanism is shown in Figure 3A. Representative SEM images taken after 0, 2, 4, 6, 8, 10, 12, and 24 h of electrolysis are presented in Figure 3B in support of the proposed mesostar growth mechanism. (Additional images are provided in the Supporting Information, Figure S6, showing an overview of the entire system at a given time period). The SEM image of nanorice particles is shown in Figure 3B-i. During electrolysis, the Au shell of nanorice particles is etched away, leaving residual Au islands and small Au colloid in the reaction mixture (Figure 3B-ii). The etching process of the Au shell may result from two plausible mechanisms. First, active O_2 is produced during electrolysis (eq 2)

which has been shown to etch Au.[16] Second, active hydroxyl groups, which are also produced during electrolysis (eq 1), may react with the hematite core, altering its crystal structure. The subsequent recrystallization of the hematite core may then induce strain on the Au shell, causing it to partially etch.[17]

$$\text{Cathode}: 2H_2O_{(l)} + 2e^- \rightarrow H_{2(g)} + 2OH^-_{(aq)} \qquad E_{red} = 0.00\text{V} \quad (1)$$

$$\text{Anode}: 4OH^-_{(aq)} \rightarrow O_{2(g)} + 2H_2O_{(l)} + 4e^- \qquad E_{ox} = -1.23\text{V}. \quad (2)$$

Active hydroxyl anions produced during electrolysis could also be incorporated into the hematite crystal lattice as hydroxyl defects, forming a metastable phase termed "hydrohematite" ($Fe_2O_3.H_2O$).[18,19] α-Fe_2O_3 possibly converts to α-FeOOH from the hydrohematite phase by replacement of oxygen atoms with hydroxyl ions:

$$2Fe_2O_3 \cdot H_2O + 2OH^- + 2H^+ \rightarrow 4FeOOH + O_2 + 2H_2 \quad (3)$$

In addition to partial removal of the Au shell, the electrolysis process partially disintegrates the α-Fe_2O_3 particles, converting them into α-FeOOH nanocrystals (see Figure 2C). Subsequent to Au shell disintegration, the partially etched nanorice particles were completely coated with α-FeOOH nanocrystals and colloidal Au particles. These structures then preferentially aligned along their centers to form a cross-shaped structure (Figure 3B-iii). In some cases, end-to-end assembly occurred and formed long chains, but these were produced in relatively low yield (see Supporting Information Figure S2). After 4 h of electrolysis, α-FeOOH nanocrystals assembled on the central axis of the cross structures, which was possibly the most convenient polarizable axis in the DC-field. This transformed the cross structures into star-shaped structures (Figure 3B iv,v). These star-shaped mesostructures continued to grow and after 24 h of electrolysis yielded hierarchical crystalline mesostars (Figure 3B vi−viii). The mesostars were formed in the bulk of solution and were not observed on the electrodes. A representative SEM image of the electrode is provided in the Supporting Information (Figure S5). Colloidal Au particles that initially disintegrated from nanorice particles were also incorporated into these complex mesostructures. The conversion yield from nanorice particles to mesostars was ~50%. Since these mesostructures are larger in size than the nanorice, and the formation of mesostars is distinct from solution phase synthesis or seeded growth method, a lower conversion yield is expected.

These observations elucidate the α-Fe_2O_3 and Au peaks observed in the XRD spectra of mesostars (Figure 1B-iii) as well as the Au SAED pattern shown in Figure 2F. The Au peaks in the XRD spectra could also be due to the residual colloidal Au particles in solution which disintegrated from the nanorice. These observations also explain the polycrystalline rings in the ED patterns (Figure 2A,F), which could be a consequence of self-assembly and oriented attachment of many α-FeOOH nanoparticles to form the mesostars.

The formation of the mesostars as a result of the specific oriented assembly of the α-FeOOH nanoparticles on the central axis of the cross structures could be due to defects in the α-FeOOH crystal structure and resulting magnetization in individual particles.[19,20] This magnetization results in weak interparticle magnetic interactions. Magnetism in α-FeOOH nanocrystals depends on several factors including the crystallinity of the particles, particle size, temperature, and surface defects. Bocquet *et al.*[12,13,21] proposed that as the size of α-FeOOH particles decreases, the number of crystal defects increases facilitating magnetic cluster ordering and reduced Neel temperature (T_N). The T_N of bulk α-FeOOH is ~398 K. The saturation magnetization val-

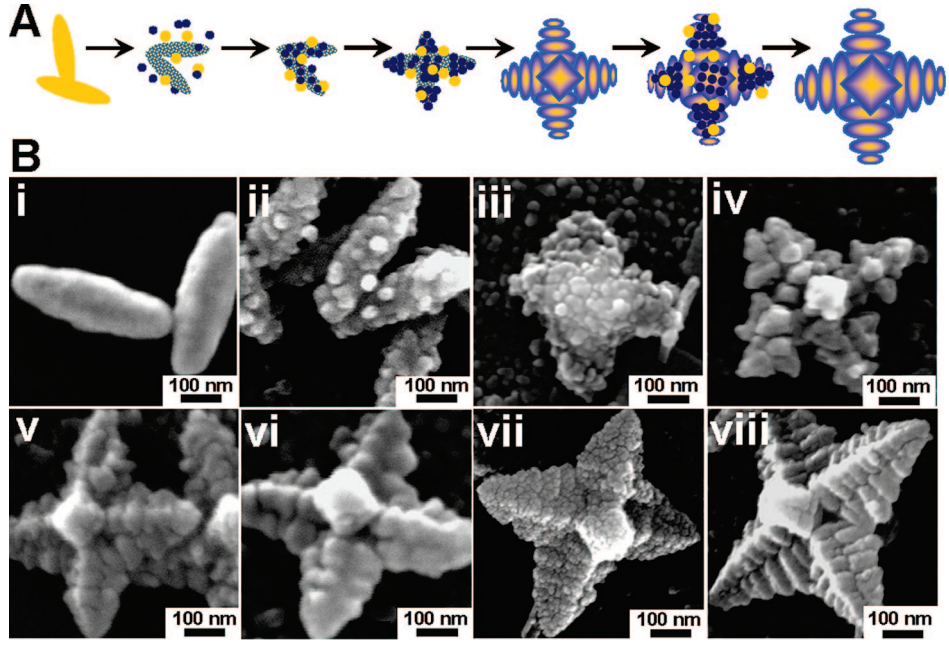

Figure 3. (A) Schematic representation of mesostar formation mechanism. (B) SEM images supporting the mesostar formation mechanism starting with (i) nanorice, (ii) 2 h of electrolysis, (iii) 4, (iv) 6, (v) 8, (vi) 10, (vii) 12, and (viii) 24 h.

ues found in nanoscale materials are usually smaller than the corresponding bulk phases, provided that no change in ionic configurations occurs. Bocquet *et al.*[12] have reported a T_N as low as ~261 K for α-FeOOH nanocrystals, which indicates they have a net magnetic moment at ambient temperature. Structural defects in α-FeOOH nanocrystals, such as iron and hydrogen vacancies, results in unpaired chains at the surface, which also contributes to a net increase in magnetization.[22,23] Thus, the formation of mesostars could have occurred because of the assembly of α-FeOOH nanocrystals along the most convenient polarizable axis in the DC-field as well as the weak interparticle magnetic interaction between the α-FeOOH nanocrystals.

A control experiment with the α-Fe_2O_3 cores without any Au shell was performed resulting in an alteration of the composition and morphology of the α-Fe_2O_3 nanoparticles. Very few pyramidal mesostructures (yield ~5%) were obtained, but mesostars were not observed (see Supporting Information Figure S3). Peaks corresponding to α-FeOOH were observed in the XRD spectrum of these pyramidal structures, which again indicate that α-Fe_2O_3 transforms into α-FeOOH *via* electrolysis in an aqueous media (see Supporting Information Figure S4). The low yield of the pyramidal structures and absence of mesostars suggest that the Au shell may act as a direct agent in initiating nucleation sites for mesostar formation and facilitating shape evolution of these hierarchical mesostructures.

The formation mechanism of these hierarchical mesostructures was further established by studying the electrolysis-assisted assembly of nanorice particles as a function of voltage. The voltage between the electrodes was varied between 0.5 and 10 V, while the reaction time (24 h) and the distance between the electrodes (0.014 m) remained constant. At both 0.5 and 1 V, only aggregated nanorice particles were obtained, but mesostars were not observed (Figure 4A). This strongly indicates that below 1.23 V, the redox potential for H_2O electrolysis, mesostar formation is not initiated. At 2 V, very few micrometer-sized star-shaped structures were observed, while most of the nanorice particles remained in solution (Figure 4B). These were large fractal structures, measuring ~4 ± 0.2 μm in length and width, and 1.1 ± 0.2 μm in height. The small yield probably occurred because fewer nucleation sites for mesostar formation were initiated at lower voltage. This resulted in slower growth kinetics, which usually favors Ostwald ripening in order to minimize the overall surface free energy, resulting in the formation of larger but fewer stars. At 3 V, slightly smaller star-shaped structures with a length and width of 3.1 ± 0.7 μm and a height of 0.8 ± 0.3 μm were obtained. As the voltage was raised to 5 V, a higher yield of mesostars with a length and width of 650 ± 80 nm and a height of 380 ± 30 nm was observed. As the voltage was further increased to 10 V, a high yield of incomplete and deformed stars 450 ± 150 nm in length were obtained. These observations indicate that at higher voltage more nucleation sites are initiated leading to a higher rate of growth kinetics. This also results in the formation of distorted star-shaped morphologies with an overall decrease in size, and a larger size distribution.

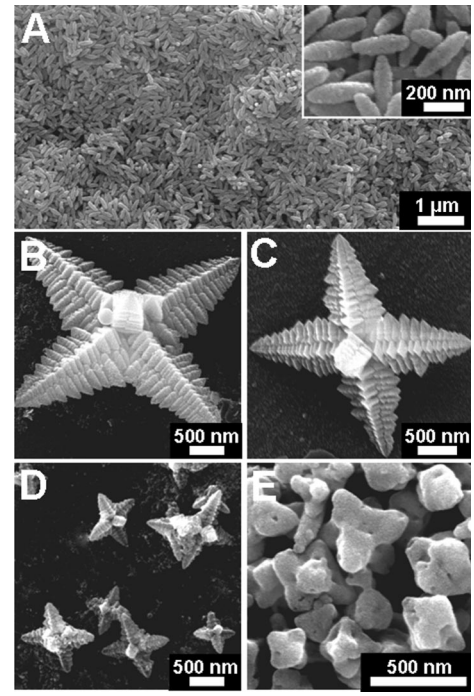

Figure 4. SEM images of mesostructures obtained by varying the voltage while keeping electrolysis time constant at 24 h: (A) aggregated nanorice formed at 0.5 and 1 V and high resolution image provided as inset; (B) stars ~4 ± 0.2 μm in length and width, and 1.1 ± 0.2 μm in height formed at 2 V; (C) stars ~3.1 ± 0.7 μm in length and width, and 0.8 ± 0.3 μm in height obtained at 3 V; (D) mesostars 650 ± 80 nm in length and width, and 380 ± 30 nm in height observed at 5 V; and (E) distorted stars 450 ± 150 nm in length observed at 10 V.

In addition to electrolysis, the resulting crystal structure of these hierarchical self-assembled mesostructures can also be interpreted in the context of nucleation, oriented attachment, and Ostwald ripening. Nucleation in the reaction mixture results in small crystalline α-FeOOH primary particles which aggregate *via* oriented attachment to form secondary particles. Oriented attachment involves self-organization of adjoining particles such that a regular crystallographic orientation is achieved followed by the joining of these particles at a planar interface. Oriented assembly usually results in single crystals, which could explain the single crystalline domains found in the mesostars (ED and SAED patterns shown in Figure 2). Several single crystalline domains then aggregate forming polycrystalline structures. The kinetics of crystal growth and coarsening strongly depend on various factors including the structure of the material, the surface chemistry of the particles resulting from the ions in the solution,

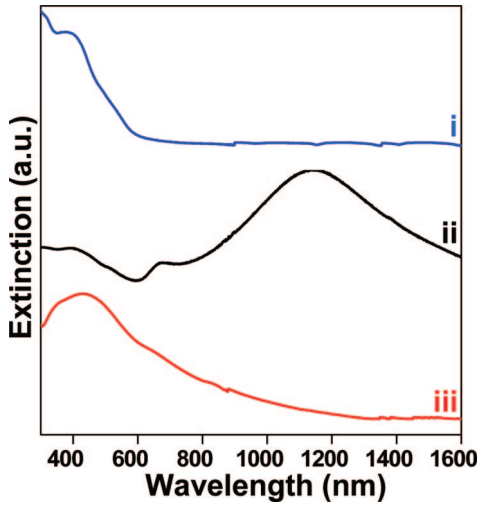

Figure 5. Extinction spectra of (i) α-Fe2O3 cores with $\lambda_{max} \approx$ 390 nm, (ii) nanorice particles with longitudinal plasmon $\lambda_{max} \approx$ 1100 nm and transverse plasmon $\lambda_{max} \approx$ 650 nm, and (iii) mesostars with $\lambda_{max} \approx$ 430 nm. The samples measured are monolayers of nanoparticles immobilized on PVP-glass slides. The spectra are offset for clarity.

and the interface between the crystals and surrounding solution.[24−26] With increasing time, Ostwald ripening controls the crystal growth by the diffusion of ions along the matrix-particle boundary resulting in larger particle sizes.[27,28] The observed morphology of the mesostars could be due to the simultaneous occurrence of adjacent particles in solution epitaxially assembling during the electrolysis process along the most convenient polarizable axis for DC-field as well as Ostwald ripening.

Since the optical properties of materials are governed by shape, size, and chemical composition, the extinction spectra of the α-Fe_2O_3 cores, Au-nanorice, and mesostars were compared using UV−vis spectroscopy (Figure 5). The extinction spectra were obtained by immobilizing the particles on quartz slides. The α-Fe_2O_3 cores showed an absorption maximum at ~390 nm, while nanorice demonstrated two separate peaks at 650 and 1100 nm. The strong plasmon resonance feature at 1100 nm was due to the longitudinal plasmon mode of the nanorice while the weaker plasmon resonance at 650 nm was due to the transverse plasmon mode of the nanorice particles. The optical spectrum of the mesostars is strikingly different from nanorice and revealed a broad peak with absorption maximum at 430 nm, which was attributable to the presence of α-Fe_2O_3, α-FeOOH, and Au. In the control experiment, the optical properties of the pyramidal mesostructures obtained with the hematite cores did not show any well-defined peak (see Supporting Information, Figure S4) which additionally signifies the contribution of Au colloidal particles in the observed optical spectra of the mesostars.

CONCLUSIONS

In conclusion, we have observed the unusual formation of hierarchical mesostars *via* electrolysis of an aqueous suspension of nanorice particles. The Au-α-Fe_2O_3 nanorice particles self-assembled into fractal mesostructures composed of α-Fe_2O_3, α-FeOOH, and Au. The remarkable differences in the geometry, composition, and properties between the nanorice particles and mesostars strongly indicate that electrolysis can significantly alter the morphology and constituent material of the nanostructures. A further examination of this striking assembly process could elucidate the unusual self-assembly processes observed in nature and biological systems. Further study of this system may be also promising in fundamental applications characteristic to hierarchical mesostructures.

METHODS

Materials. Ferric chloride ($FeCl_3.6H_2O$), (3-aminopropyl) triethoxysilane (APTES, 99%), tetrachloroauric acid ($HAuCl_4.3H_2O$), tetrakis hydroxymethyl phosphonium chloride (THPC), polyvinyl pyridine (PVP) were purchased from Sigma-Aldrich (St. Louis, MO). Formaldehyde (37%), sulfuric acid (H_2SO_4, 100%), hydrogen peroxide (H_2O_2, 30%), potassium dihydrogen phosphate (KH_2PO_4) and 200-proof ethanol were obtained from Fisher Scientific (Hampton, NH). All the chemicals were used as received without further purification. Platinum electrodes and platinum wire were purchased from Alfa Aesar. DC power supply was purchased from Hewlett-Packard. Quartz slides were purchased from Technical Glass.

Nanorice Fabrication. Monodisperse spindle-shaped α-Fe_2O_3 nanoparticles and nanorice particles were fabricated as previously reported.[9,29] Briefly, α-Fe_2O_3 particles with an aspect ratio of 6.3 (340 nm × 54 nm) were prepared by forced hydrolysis of ferric chloride solutions by reacting 100 mL of an aqueous mixture containing 2.0×10^{-2} M $FeCl_3$ and 4.0×10^{-4} M KH_2PO_4 at 100 °C for 72 h. The resulting precipitate was centrifuged and washed several times with water and ethanol and finally redispersed in 20 mL of ethanol. The surface of the α-Fe_2O_3 particles was functionalized with organosilane molecules (APTES) to generate an amine-terminated surface. This was achieved by mixing 500 μL of APTES with 5 mL of ethanolic solution of hematite particles for 12 h under vigorous stirring. The resulting particles were centrifuged and redispersed in ethanol several times to remove excess APTES. These functionalized nanoparticles were decorated with small gold colloid (2−3 nm) prepared by the method reported by Duff *et al.*[30] Nanorice particles were fabricated *via* seed-mediated reduction of $AuCl_4^-$ ions onto the attached small colloid in the presence of formaldehyde.

Nanoparticle Films for Optical Measurements. Nanoparticle films were obtained by immobilizing them on PVP-functionalized quartz slides. Briefly, quartz slides were cleaned in piranha solution (H_2SO_4 (100%):H_2O_2 (30%) = 3:1) for 2 h, rinsed with H_2O and 200 proof-ethanol and dried in a stream of N_2 gas. The slides were then immersed in a 1 wt % solution of PVP in ethanol for 24 h, followed by rinsing thoroughly in ethanol and drying with N_2 gas. The PVP-functionalized slides were immersed in aqueous solutions of nanorice, mesostars, hematite nanoparticles, and pyramidal mesostructures for 1 h. Upon removal from the individual solutions, the slides were rinsed with ethanol and dried with N_2 gas. This resulted in a monolayer of randomly oriented nanoparticles on the PVP-functionalized slides.

Characterization. The nanoparticles were characterized by obtaining TEM images using a JEOL JEM-2010 TEM operated at 200 kV, SEM images using a FEI Quanta 400 field emission SEM at an acceleration voltage of 20 kV, XRD patterns by using a Rigaku Ultima II vertical θ-θ powder diffractometer (Cu Kα, λ = 1.5418 Å), and absorption measurements using a Varian Cary 5000 UV−vis−NIR spectrophotometer.

Acknowledgment. We gratefully acknowledge the Robert A. Welch Foundation (C-1220) and MURI (W911NF-04-01-0203) for financial support. We thank Lisa Brown, Carly Levin, Surbhi Lal, and Bruce Brinson for helpful discussions.

Supporting Information Available: XRD spectra and corresponding powder diffraction intensity profiles of mesostars, hematite nanoparticles, and nanorice; SEM image of long chain branched structures; SEM images of pyramidal mesostructures; XRD spectra and absorption spectra of pyramidal mesostructures; SEM images of electrodes utilized in electrolytic cell; additional SEM images supporting mesostar formation mechanism. This material is available free of charge *via* the Internet at http://pubs.acs.org.

REFERENCES AND NOTES

1. Huang, M. C. Y.; Zhou, Y.; Chang-Hasnain, C. J. A Nanoelectromechanical Tunable Laser. *Nat. Photonics* **2008**, *2*, 180–184.
2. Caruge, J. M.; Halpert, J. E.; Wood, V.; Bulović, V.; Bawendi, M. G. Colloidal Quantum-Dot Light-Emitting Diodes with Metal-Oxide Charge Transport Layers. *Nat. Photonics* **2008**, *2*, 247–250.
3. Mack, N. H.; Wackerly, J. W.; Malyarchuk, V.; Rogers, J. A.; Moore, J. S.; Nuzzo, R. G. Optical Transduction of Chemical Forces. *Nano Lett.* **2007**, *7*, 733–737.
4. Lal, S.; Link, S.; Halas, N. J. Nano-optics from Sensing to Waveguiding. *Nat. Photonics* **2007**, *1*, 641–648.
5. Parker, A. R.; Townley, H. E. Biomimetics of Photonic Nanostructures. *Nat. Nanotechnol.* **2007**, *2*, 347–353.
6. Tang, L.; Shi, L.; Bonneau, C.; Sun, J.; Yue, H.; Ojuva, A.; Lee, B. L.; Kritikos, M.; Bell, R. G.; Bacsik, Z.; Mink, J.; Zou, X. A Zeolite Family with Chiral and Achiral Structures Built from the Same Building Layer. *Nat. Mater.* **2008**, *7*, 381–385.
7. Gao, L.; Zhuang, J.; Nie, L.; Zhang, J.; Zhang, Y.; Gu, N.; Wang, T.; Feng, J.; Yang, D.; Perrett, S.; Yan, X. Intrinsic Peroxidase-like Activity of Ferromagnetic Nanoparticles. *Nat. Nanotechnol.* **2007**, *2*, 577–583.
8. Ladet, S.; David, L.; Domard, A. Multi-Membrane Hydrogels. *Nature* **2008**, *452*, 76–80.
9. Wang, H.; Brandl, D. W.; Le, F.; Nordlander, P.; Halas, N. J. Nanorice: A Hybrid Plasmonic Nanostructure. *Nano Lett.* **2006**, *6*, 827–832.
10. Thorp, J. C.; Sieradzki, K.; Tang, L.; Crozier, P. A.; Misra, A.; Nastasi, M.; Mitlin, D.; Picraux, S. T. Formation of nanoporous noble metal thin films by electrochemical dealloying of Pt_xSi_{1-x}. *Appl. Phys. Lett.* **2006**, *88*, 033110−-1–033110-3.
11. Yang, D.; Meng, G.; Zhang, S.; Hao, Y.; An, X.; Wei, Q.; Yeab, M.; Zhang, L. Electrochemical Synthesis of Metal and Semimetal Nanotube−nanowire Heterojunctions and Their Electronic Transport Properties. *Chem. Commun.* **2007**, *17*, 1733–1735.
12. Bocquet, S.; Pollard, R. J.; Cashion, J. D. Dynamic Magnetic Phenomena in Fine-Particle Goethite. *Phys. Rev. B* **1992**, *46*, 11657–11664.
13. Bocquet, S.; Hill, A. J. Correlation of Neel Temperature and Vacancy Defects in Fine-Particle Goethites. *Phys. Chem. Miner.* **1995**, *22*, 524–528.
14. Li, S.; Zhang, H.; Wu, J.; Ma, X.; Yang, D. Shape-Control Fabrication and Characterization of the Airplane-like FeO(OH) and Fe_2O_3 Nanostructures. *Cryst. Growth Des.* **2006**, *6*, 351–353.
15. Chen, R.; Chen, H.; Wei, Y.; Hou, D. Photocatalytic Oxidation of $Fe(OH)_2$ Suspension with Visible Light Irradiation. *J. Phys. Chem. C* **2007**, *111*, 16453–16459.
16. Wang, H.; Goodrich, G. P.; Tam, F.; Oubre, C.; Nordlander, P.; Halas, N. J. Controlled Texturing Modifies the Surface Topography and Plasmonic Properties of Au Nanoshells. *J. Phys. Chem. B* **2005**, *109*, 11083–11087.
17. Bae, D. H.; Lee, M. H.; Kim, K. T.; Kim, W. T.; Kim, D. H. Application of Quasicrystalline Particles As a Strengthening Phase in Mg−Zn−Y Alloys. *J. Alloys Compd.* **2002**, *342*, 445–450.
18. Chernyshova, I. V.; Hochella, M. F. J.; Madden, A. S. Size-Dependent Structural Transformations of Hematite Nanoparticles. 1. Phase Transition. *Phys. Chem. Chem. Phys.* **2007**, *9*, 1736–1750.
19. Pomiès, M. P.; Morin, G.; Vignaud, C. XRD Study of the Goethite-Hematite Transformation: Application to the Identification of Heated Prehistoric Pigments. *Eur. J. Solid State Inorg. Chem.* **1998**, *35*, 9–25.
20. Morup, S.; Madsen, M. B.; J., F. A New Interpretation Of Mossbauer Spectra Of Microcrystalline Goethite: "Superferromagnetism" Or "Super-Spin-Glass" Behaviour? *J. Magn. Magn. Mater* **1983**, *40*, 163–174.
21. Bocquet, S.; Kennedy, S. J. The Néel Temperature of Fine Particle Goethite. *J. Magn. Magn. Mater.* **1992**, *109*, 260–264.
22. Guyodo, Y.; Mostrom, A.; Penn, R. L.; Banerjee, S. K. From Nanodots to Nanorods: Oriented Aggregation and Magnetic Evolution of Nanocrystalline Goethite. *Geophys. Res. Lett.* **2003**, *30*, 19−119−4.
23. Barrero, C. A.; Betancur, J. D.; Greneche, J. M.; Goya, G. F.; Berquo, T. S. Magnetism in Nonstoichiometric Goethite of Varying Total Water Content and Surface Area. *Geophys. J. Int.* **2006**, *164*, 331–339.
24. Ahniyaz, A.; Sakamoto, Y.; Bergstrom, L. Magnetic Field-Induced Assembly of Oriented Superlattices from Maghemite Nanocubes. *Proc. Nat. Acad. Sci. U.S.A.* **2007**, *104*, 17570–17574.
25. Li, W.-J.; Shi, E.-W.; Zhong, W.-Z.; Yin, Z.-W. Growth Mechanism and Growth Habit of Oxide Crystals. *J. Cryst. Growth* **1999**, *203*, 186–196.
26. Penn, R. L.; Stone, A. T.; Veblen, D. R. Defects and Disorder: Probing the Surface Chemistry of Heterogenite (CoOOH) by Dissolution Using Hydroquinone and Iminodiacetic Acid. *J. Phys. Chem. B* **2001**, *105*, 4690–4697.
27. Banfield, J. F.; Welch, S. A.; Zhang, H.; Ebert, T. T.; Penn, R. L. Aggregation-Based Crystal Growth and Microstructure Development in Natural Iron Oxyhydroxide Biomineralization Products. *Science* **2000**, *289*, 751–754.
28. Penn, R. L.; Banfield, J. F. Imperfect Oriented Attachment: Dislocation Generation in Defect-Free Nanocrystals. *Science* **1998**, *281*, 969–971.
29. Ozaki, M.; Kratohvil, S.; Matijevic, E. Formation of Monodispersed Spindle-Type Hematite Particles. *J. Colloid Interface Sci.* **1984**, *102*, 146–151.
30. Duff, D. G.; Baiker, A.; Edwards, P. P. A New Hydrosol of Gold Clusters. 1. Formation and Particle Size Variation. *Langmuir* **1993**, *9*, 2301–2309.